

# MID AND FAR INFRARED PROPERTIES OF A COMPLETE SAMPLE OF LOCAL AGNS

KOHEI ICHIKAWA<sup>1</sup>, YOSHIHIRO UEDA<sup>1</sup>, YUICHI TERASHIMA<sup>2</sup>, SHINKI OYABU<sup>3</sup>, POSHAK GANDHI<sup>4</sup>, KEIKO MATSUTA<sup>5</sup>, AND  
 TAKAO NAKAGAWA<sup>4</sup>

<sup>1</sup> Department of Astronomy, Graduate School of Science, Kyoto University, Kitashirakawa-Oiwake cho, Kyoto, 606-8502, Japan

<sup>2</sup> Department of Physics, Faculty of Science, Ehime University, Matsuyama 790-8577, Japan

<sup>3</sup> Graduate School of Science, Nagoya University, Furo-cho, Chikusa-ku, Nagoya, Aichi 464-8602 Japan

<sup>4</sup> Institute of Space and Astronautical Science (ISAS), Japan Aerospace Exploration Agency, 3-1-1 Yoshinodai, Chuo-ku, Sagamihara, Kanagawa 252-5210, Japan

<sup>5</sup> Department of Space and Astronautical Science, The Graduate University for Advanced Studies, 3-1-1 Yoshinodai, Chuo-ku, Sagamihara, Kanagawa 252-5210, Japan

*Draft Version May 24, 2012*

## ABSTRACT

We investigate the mid- (MIR) to far-infrared (FIR) properties of a nearly complete sample of local Active Galactic Nuclei (AGNs) detected in the *Swift*/BAT all sky hard X-ray (14–195 keV) survey, based on the cross correlation with the *AKARI* infrared survey catalogs complemented by those with *IRAS* and *WISE*. Out of 135 non-blazar AGNs in the *Swift*/BAT 9 month catalog, we obtain the MIR photometric data for 128 sources either in the 9, 12, 18, 22, and/or 25  $\mu\text{m}$  band. We find good correlation between their hard X-ray and MIR luminosities over 3 orders of magnitude ( $42 < \log \lambda L_{\lambda}(9, 18 \mu\text{m}) < 45$ ), which is tighter than that with the FIR luminosities at 90  $\mu\text{m}$ . This suggests that thermal emission from hot dusts irradiated by the AGN emission dominate the MIR fluxes. Both X-ray unabsorbed and absorbed AGNs follow the same correlation, implying isotropic infrared emission, as expected in clumpy dust tori rather than homogeneous ones. We find excess signals around 9  $\mu\text{m}$  in the averaged infrared spectral energy distribution from heavy obscured “new type” AGNs with small scattering fractions in the X-ray spectra. This could be attributed to the PAH emission feature, suggesting that their host galaxies have strong starburst activities.

*Subject headings:* galaxies: active — galaxies: nuclei — infrared: galaxies

## 1. INTRODUCTION

A complete survey of Active Galactic Nuclei (AGNs) throughout the history of the universe is one of main goals in modern astronomy, which is necessary to understand the evolution of supermassive black holes (SMBHs) in galactic centers and their host galaxies. Given the fact that the majority of AGNs are obscured by dust and gas surrounding the SMBH, observations in hard X-ray and mid-infrared (MIR) bands are proposed to be promising tools for detecting the whole populations of AGNs (both radio quiet and loud ones) thanks to their strong penetrating power than optical/UV lights and soft X-rays. In fact, recent deep multi-wavelengths surveys utilizing these energy bands are discovering a large number of obscured AGNs (Brandt & Hasinger 2005). Hard X-ray selection gives the most efficient way to have a clean AGN sample with little contamination from host galaxies. On the other hand, MIR selection sometimes achieves even better sensitivities in detecting AGN candidates than currently available X-ray data below 10 keV for heavily Compton thick AGNs with column densities of  $N_{\text{H}} > 10^{24} \text{ cm}^{-2}$ , although separation of AGN components from star forming activities could always become an issue (Oyabu et al. 2011). To understand the efficiency and completeness of these surveys at different wavelengths, it is quite important to establish the relation between hard X-rays and infrared emission of AGNs based on a large sample of nearby, bright AGNs for which detailed studies can be made.

The *Swift*/Burst Alert Telescope (BAT) survey

(Tueller et al. 2008) is one of the most sensitive all sky surveys in the hard X-ray band ( $>10 \text{ keV}$ ), providing us with the least biased sample of AGNs in the local universe including heavily obscured ones, along with those by INTEGRAL (Winkler et al. 2003; Bird et al. 2010). *Suzaku* follow-up observations of BAT AGNs have discovered a new type of deeply buried AGNs with a very small scattering fraction (Ueda et al. 2007; Eguchi et al. 2009; Winter et al. 2009a). Assuming that the amount of gas responsible for scattering is not much different from other objects, it is suggested that these new type AGNs are obscured in a geometrically thick torus with a small opening angle. Understanding the nature of this population is important to reveal their roles in the cosmological evolution of SMBHs and host galaxies.

The MIR band also provides crucial information on the inner region of the AGN tori. It is known that a thermal continuum in the MIR band originates from hot circumnuclear dust heated by optical/UV/X-ray photons from the central engine. Many works suggest that MIR emission is a good indicator of AGN activity. Horst et al. (2008); Gandhi et al. (2009) have found a strong correlation between X-ray (2–10 keV) and MIR (12.3  $\mu\text{m}$ ) luminosity from the nucleus of Seyfert galaxies, using the VLT/VISIR data where the AGN can be spatially resolved from the host galaxy in many cases. In this paper, we statistically examine the correlation between the infrared and X-ray luminosities of AGNs by utilizing a large uniform sample in the local universe, and investigate their infrared properties as a function of obscuration type. For this purpose, we use the *Swift*/BAT 9-month catalog (Tueller et al. 2008) as the parent sam-

ple, whose multiwavelength properties have been intensively investigated. Here we focus only on “non-blazar” AGNs. As for the infrared data, we primarily use the all-sky survey catalogs obtained with *AKARI*, Japanese first infrared astronomical satellite launched on 2006 February 22 (Murakami et al. 2007), which provide unbiased galaxy samples selected in the mid- and far-infrared (FIR) bands with unprecedented sensitivities as an all sky survey mission. To complement the infrared data of AGNs whose counterparts are not detected or do not have reliable flux measurements with *AKARI*, we also utilize the all sky survey catalog of NASA’s Wide-field Infrared Survey Explorer (WISE; Wright et al. 2010) mission, launched in 2010, as well as the catalogs of the Infrared Astronomical Satellite (IRAS; Neugebauer et al. 1984), a joint project of the US, UK, and the Netherlands launched on January 25, 1983. In Section 2, we present the sample selection criteria and the results of cross correlation between the Swift/BAT and AKARI catalogs. In Section 3, we discuss our two main results, the luminosity correlations and infrared average SED for different types. The conclusion and summary are given in section 4. Throughout the paper, we adopt  $H_0 = 70.0$  km s $^{-1}$  Mpc $^{-1}$ ,  $\Omega_M = 0.3$ , and  $\Omega_\Lambda = 0.7$ .

## 2. SAMPLE

### 2.1. Swift/BAT Hard X-ray Catalog

The Swift/BAT 9-month catalog (Tueller et al. 2008) contains 137 non-blazar AGNs with a flux limit of  $2 \times 10^{-11}$  erg cm $^{-2}$  s $^{-1}$  in the 14–195 keV band. The redshift range of this sample is  $0 < z < 0.156$ . Winter et al. (2009a) investigated the soft X-ray (0.5–10 keV) properties of 128 (94.8%) BAT-detected non-blazar AGNs of Tueller et al. (2008). By fitting the X-ray spectra taken with *Swift*/X-Ray Telescope (XRT) or *XMM-Newton*, they derive key spectral parameters, such as the absorption column density ( $N_H$ ), covering fraction of the absorber ( $f_c$ ) or the scattering fraction ( $f_s$ ) with respect to the transmitted component ( $f_{\text{scat}} \simeq 1 - f_c$ ). In our paper, we do not use the interacting galaxies NGC 6921 and MCG +04-48-002, which are not separated in the Swift/BAT catalog. Hence, the parent sample consists of 135 sources.

### 2.2. Infrared Catalogs

#### 2.2.1. AKARI Point Source Catalogs

To obtain the infrared band properties of these Swift/BAT AGNs, we mainly use the *AKARI* All-Sky Survey Point Source Catalogs (AKARI-PSC). *AKARI* carries two instruments, the infrared camera (IRC; Onaka et al. 2007) for the 2–26  $\mu$ m band (centered at 9  $\mu$ m and 18  $\mu$ m) and the Far-Infrared Surveyor (FIS; Kawada et al. 2007) for the 50–200  $\mu$ m band (centered at 65, 90, 140, and 160  $\mu$ m). One of the major objective of *AKARI* satellite is to obtain an all-sky map of infrared sources. The *AKARI* all-sky survey observations covered nearly the full sky ( $\geq 96\%$ ), and detected 870,973 sources with the IRC and 427,071 sources with the FIS. It achieved the flux sensitivities of 0.05, 0.09, 2.4, 0.55, 1.4, and 6.3 Jy with position accuracies of 6 arcsec at the 9, 18, 65, 90, 140, and 160  $\mu$ m bands, respectively. In our study, we only utilize sources with the quality flag of  $FQUAL = 3$ , whose flux measurements are re-

liable<sup>1</sup>. As for the FIS catalog, we only refer to the 90  $\mu$ m data as a representative FIR flux, which achieve the most significant sensitivity improvement compared with the previous *IRAS* mission among the four FIR bands.

#### 2.2.2. IRAS Catalogs

The IRAS mission performed an unbiased all sky survey at the 12, 25, 60 and 100  $\mu$ m bands. The typical position accuracy at 12 and 25  $\mu$ m is 7 arcsec and 35 arcsec in the scan and cross scan direction, respectively (Beichman et al. 1988). In this paper we use two largest catalogs, the IRAS Point Source Catalog (IRAS-PSC) and the IRAS Faint Source Catalog (IRAS-FSC). IRAS achieved  $10\sigma$  point source sensitivities better than 0.7 Jy over the whole sky. The IRAS-FSC contains even fainter sources with fluxes of  $>0.2$  Jy in the 12 and 25  $\mu$ m bands. We use only IRAS sources with  $FQUAL = 3$  (the highest quality)<sup>2</sup>.

#### 2.2.3. WISE All-Sky Catalog

The WISE mission mapped the sky at the 3.4, 4.6, 12, and 22  $\mu$ m bands, achieving  $5\sigma$  point source sensitivity better than 0.08, 0.11, 1, and 6 mJy, respectively, in unconfused regions on the ecliptic poles (Wright et al. 2010). The WISE all-sky survey utilizes the data taken from 2010 January 7 to August 6<sup>3</sup>. The source catalog contains positional and photometric information for over 563 million objects. The position accuracy estimated from the comparison with the 2MASS catalog is  $\sim 2$  arcsec at  $3\sigma$  level. In this paper, we only use sources with the flux quality indicator  $ph\_qual = A$ , which has Signal-to-Noise ratio larger than 10. Since the angular resolutions of WISE (6.5 and 12.0 arcsec at 12 and 22  $\mu$ m, respectively) are slightly worse than those of *AKARI* IRC (5.5 and 5.7 arcsec at 9 and 18  $\mu$ m, respectively), we refer to the profile-fitting photometry of WISE derived by assuming point-like sources, for consistency with the *AKARI* catalog. This is justified because our targets of WISE are relatively distant (hence more compact) compared with those detected with *AKARI* or *IRAS* (see Section 2.3 for details). The photometric data of WISE are given in Vega magnitude, from which we convert into the Jan-sky unit using the zero-point flux densities of  $F_{\nu}(\text{iso}) = 31.674$  Jy and 8.363 Jy for 12  $\mu$ m and 22  $\mu$ m, respectively.

### 2.3. Cross Correlation of Swift/BAT AGNs with the IR Catalogs

We determine the IR counterparts of the Swift/BAT AGNs by cross-correlating the *AKARI*, *IRAS*, and *WISE* catalogs in this order. Our primary goal is to obtain the photometric data in the MIR band as completely as possible from the hard X-ray selected sample. We put the highest priority to the *AKARI* catalog because of its high sky coverage (97 % of the all sky) and 2–4 times

<sup>1</sup> See the release note of the *AKARI*/FIS catalog for the details of  $FQUAL$ . It is recommended not to use the flux data when  $FQUAL \leq 2$  for a reliable scientific analysis.

[http://irsa.ipac.caltech.edu/data/AKARI/documentation/AKARI-FIS\\_BSC\\_V1](http://irsa.ipac.caltech.edu/data/AKARI/documentation/AKARI-FIS_BSC_V1)

<sup>2</sup> see Beichman et al. (1988) for the definition of  $FQUAL$  in the *IRAS* catalogs. False detections may be included when  $FQUAL \leq 2$ .

<sup>3</sup> see the release note of WISE,  
<http://wise2.ipac.caltech.edu/docs/release/allsky/>

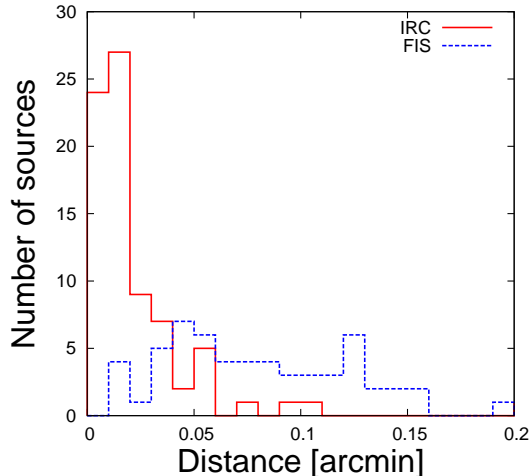


FIG. 1.— The histograms of position difference between the optical counterparts of the Swift/BAT AGNs and their AKARI counterparts (red solid line: IRC, blue dashed line: FIS).

higher sensitivity than the IRAS survey. While all the IRAS sources should be detected with AKARI, AKARI’s flux quality flags of very nearby ( $z < 0.005$ ) objects turn out to be bad due to their extended morphology when fitted with a single Gaussian. In such cases, we rather refer to the IRAS data with good flux quality, which have  $\approx 11$  times worse angular resolution than AKARI, since we aim to measure the total MIR flux from both nucleus and host galaxy in a uniform way for all the AGN sample. For AGNs that are not detected with AKARI or IRAS, we utilize the WISE all-sky catalog, which has 50 times better sensitivity than AKARI and therefore we can search fainter sources than ever in the MIR all-sky view, although the bright source are saturated due to the high sensitivity.

First, based on the positional matching of the optical counterparts of the Swift/BAT AGNs with the AKARI-PSC, we determine their infrared counterparts in the 9  $\mu\text{m}$ , 18  $\mu\text{m}$ , and 90  $\mu\text{m}$  bands. Here we adopt the maximum angular separation of 0.15’ and 0.2’ for the IRC and FIS sources, respectively, which correspond to typical  $3\sigma$  positional errors at faintest fluxes (Ishihara et al. 2010; Yamamura et al. 2010). We find 70, 79, and 62 AKARI counterparts in the 9  $\mu\text{m}$ , 18  $\mu\text{m}$ , and 90  $\mu\text{m}$  bands out of the total 135 non-blazar BAT AGN sample. Figure 1 shows the distribution of the angular separation between AKARI and optical positions for the Swift/BAT AGNs with IRC counterparts (red) and those with FIS counterparts (blue). The IRC sources are more concentrated in a small distance range (with an average of  $\langle \Delta r \rangle = 0.02'$ ) than the FIS sources ( $\langle \Delta r \rangle = 0.08'$ ), as expected from the positional accuracy in these catalogs.

Further, for AGNs whose MIR fluxes are not reliably measured ( $FQUAL < 3$ ) or not detected with AKARI (65 and 56 sources in the 9  $\mu\text{m}$  and 18  $\mu\text{m}$ ), we search for their counterparts at 12  $\mu\text{m}$  or 25  $\mu\text{m}$  in the IRAS-FSC and IRAS-PSC. Here we adopt the 50 arcsec radius, corresponding to the  $< 2\sigma$  positional error in the cross-scan direction. As a result, 11 and 9 IRAS counterparts with  $FQUAL = 3$  are identified in the 12  $\mu\text{m}$  and 25  $\mu\text{m}$  band, respectively. Finally, we utilize the the WISE catalog to find the MIR counterparts in the 12  $\mu\text{m}$  or 22  $\mu\text{m}$  band for the remaining AGNs detected neither in the

AKARI nor IRAS catalogs (54 and 47 sources in the 9  $\mu\text{m}$  and 18  $\mu\text{m}$  bands). The matching radius of 2 arcsec is adopted. Thus, we identify 45 and 39 WISE sources with  $ph\_qual = A$  in the 12  $\mu\text{m}$  and 22  $\mu\text{m}$  band, respectively. In summary, we identify total 128 MIR counterparts detected any in the 9, 12, 18, 22, and 25  $\mu\text{m}$  out of the 135 Swift/BAT AGNs. Thus, the completeness of identification in the MIR band is 95%.

We confirm that the probability of wrong identification with unassociated IR sources is negligible with these criteria for all the IR catalogs. Since the mean number density of the AKARI-PSC IRC and FIS sources in the all sky is  $\sim 20 \text{ deg}^{-2}$  and  $\sim 10 \text{ deg}^{-2}$ , the expected number of contamination for the total 135 AGNs within each error circle is estimated to be only 0.05 and 0.04, respectively. The number density in the IRAS catalog is  $6.2 \text{ deg}^{-2}$ , and hence the expected contamination for the 65 AGNs whose counterparts are searched for within the radius of 50 arcsec is 0.24. Similarly, we estimate false identification of the WISE sources with a number density of  $5.63 \times 10^8 / (4.125 \times 10^4) = 1.36 \times 10^4 \text{ deg}^{-2}$  to be 0.71 within the radius of 2 arcsec for the searched 54 sources.

#### 2.4. AGN Type

To examine the infrared properties for different AGN populations, we divide the sample into three types based on the X-ray spectra. The first one is “X-ray type-1” (hereafter type-1) AGNs, defined as those showing the absorption column density of  $N_{\text{H}} < 10^{22} \text{ cm}^{-2}$ . The second is “X-ray type-2” (hereafter type-2) AGNs that have  $N_{\text{H}} > 10^{22} \text{ cm}^{-2}$ . In addition, we are interested in whether or not there is distinction in the IR properties of “new type” AGNs, which exhibit extremely small scattered fraction ( $f_{\text{scat}} \equiv 1 - f_c$ ) suggesting the geometrically thick tori around the nuclei. Here we define new type AGNs as those satisfying  $f_c \geq 0.995$ , which are treated separately from the other (normal) type-2 AGNs in this paper.

#### 2.5. Luminosity Correlation between AKARI, IRAS, and WISE Data

To make it possible to uniformly treat the MIR luminosities of AGNs at slightly different wavelengths obtained from the three IR observatories, we here investigate the correlation between the AKARI/IRAS/WISE luminosities, using the sample commonly detected with AKARI and IRAS, or with AKARI and WISE. We choose IRAS 12  $\mu\text{m}$ /WISE 12  $\mu\text{m}$  for AKARI 9  $\mu\text{m}$ , and IRAS 25  $\mu\text{m}$ /WISE 22  $\mu\text{m}$  for AKARI 18  $\mu\text{m}$ , respectively, because of the proximity of the central wavelengths. Figure 2 displays luminosity correlations between (1) AKARI 9  $\mu\text{m}$  versus IRAS 12  $\mu\text{m}$ , (2) AKARI 9  $\mu\text{m}$  versus WISE 12  $\mu\text{m}$ , (3) AKARI 18  $\mu\text{m}$  versus IRAS 25  $\mu\text{m}$ , and (4) AKARI 18  $\mu\text{m}$  versus WISE 22  $\mu\text{m}$ . We check the strength of these luminosity correlations by using Spearman’s test. We obtain Spearman Rank coefficient ( $\rho$ ) and null hypothesis probability  $P$  of (1)  $(\rho, P) = (0.97, 2.37 \times 10^{-34})$ , (2)  $(\rho, P) = (0.97, 3.6 \times 10^{-37})$ , (3)  $(\rho, P) = (0.98, 5.7 \times 10^{-40})$ , and (4)  $(\rho, P) = (0.99, \leq 10^{-42})$ . Since correlations between “luminosities” can be forced from those between “fluxes”, we also check the strength of the flux-flux correlations and obtain (1)  $(\rho, P) = (0.93, 7.6 \times 10^{-24})$ , (2)  $(\rho, P) = (0.92, 4.9 \times 10^{-26})$ , (3)  $(\rho, P) = (0.96, 5.9 \times 10^{-33})$ , and



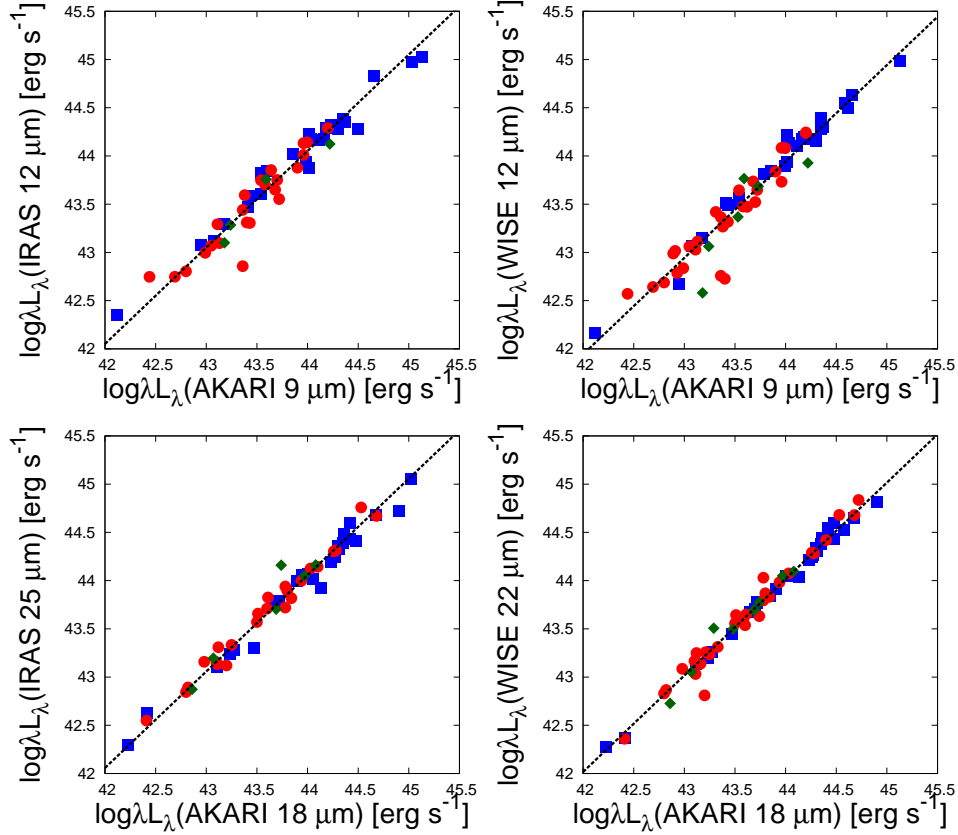


FIG. 2.— Correlation plots of infrared luminosities between AKARI 9  $\mu\text{m}$  and IRAS 12  $\mu\text{m}$  (top left, 53 sample), AKARI 9  $\mu\text{m}$  and WISE 12  $\mu\text{m}$  (top right, 61 sample), AKARI 18  $\mu\text{m}$  and IRAS 25  $\mu\text{m}$  (bottom left, 56 sample), and AKARI 18  $\mu\text{m}$  and WISE 22  $\mu\text{m}$  (bottom right, 70 sample). Squares (blue) represent type-1 AGNs ( $N_{\text{H}} < 10^{22} \text{cm}^{-2}$ ), circles (red) type-2 AGNs ( $N_{\text{H}} \geq 10^{22} \text{cm}^{-2}$ ), and diamonds (green) new type AGNs. The regression lines are given by eqs. (1), (2), (3), and (4) in Section 2.5.

(4)  $(\rho, P) = (0.99, \leq \times 10^{-42})$ . Thus, we confirm that the correlations in both luminosity and flux between different infrared catalogs are tight and significant. The standard deviation of the luminosity-ratio distribution between these two bands in the logarithm scale is found to be (1) 0.14 dex, (2) 0.17 dex, (3) 0.10 dex, and (4) 0.08 dex, respectively. The dispersion does not affect our conclusion on the MIR and hard X-ray luminosity correlation (Section 3.1). Based on the correlation, we derive the empirical formula to convert the IRAS or WISE luminosities at 12  $\mu\text{m}$ , 22  $\mu\text{m}$ , or 25  $\mu\text{m}$  into the equivalent AKARI luminosities at 9  $\mu\text{m}$  or 18  $\mu\text{m}$  as follows;

$$\log \lambda L_{\lambda}(\text{AKARI } 9 \mu\text{m}) = \log \lambda L_{\lambda}(\text{IRAS } 12 \mu\text{m}) - 0.051 \quad (1)$$

$$\log \lambda L_{\lambda}(\text{AKARI } 9 \mu\text{m}) = \log \lambda L_{\lambda}(\text{WISE } 12 \mu\text{m}) + 0.057 \quad (2)$$

$$\log \lambda L_{\lambda}(\text{AKARI } 18 \mu\text{m}) = \log \lambda L_{\lambda}(\text{IRAS } 25 \mu\text{m}) - 0.058 \quad (3)$$

$$\log \lambda L_{\lambda}(\text{AKARI } 18 \mu\text{m}) = \log \lambda L_{\lambda}(\text{WISE } 22 \mu\text{m}) - 0.016 \quad (4)$$

Assuming that AGNs detected not with AKARI but with IRAS or WISE should follow the same correlations as examined here, we apply these conversion factors to derive the 9 or 18  $\mu\text{m}$  “AKARI equivalent” luminosities for them so that we can discuss the correlation with hard X-rays in a uniform way regardless of the matched catalogs. Among the 128 Swift/BAT AGNs with MIR coun-

terparts, 126 and 127 objects have the flux measurement in the 9  $\mu\text{m}$  and 18  $\mu\text{m}$  band, respectively. The 9  $\mu\text{m}$  sample consists of 70 AKARI sources, 11 IRAS sources, and 45 WISE sources (126 sources in total), while the 18  $\mu\text{m}$  sample consists of 79 AKARI sources, 9 IRAS sources, and 39 WISE sources (127 sources in total). The summed sample detected either in the 9  $\mu\text{m}$ , 18  $\mu\text{m}$ , or AKARI 90  $\mu\text{m}$  band consists of 128 sources (9  $\mu\text{m}$ ; 126, 18  $\mu\text{m}$ ; 127, 90  $\mu\text{m}$ ; 62).

## 2.6. Basic Properties of the Sample

Figure 3 displays the redshift distribution of the 128 AGNs with MIR counterparts (blue) together with that of the whole (Tueller et al. 2008) sample of 135 AGNs (red). Since our sample is highly complete (95%), we regard our current sample with MIR counterparts as representative of the whole population of hard X-ray selected AGNs, and hereafter ignore any issues related to the incompleteness. Table 1 summarizes the infrared to X-ray properties of all the 135 Swift/BAT 9 month non-blazar AGNs in Tueller et al. (2008), including 128 objects with MIR counterparts: (1) source No. in Tueller et al. (2008), (2) object name, (3) redshift, (4)–(6) infrared fluxes ( $F_{\nu}$ ) at 9  $\mu\text{m}$ , 18  $\mu\text{m}$ , and 90  $\mu\text{m}$ , (7)–(9) infrared luminosities ( $\lambda L_{\lambda}$ ) at 9  $\mu\text{m}$ , 18  $\mu\text{m}$ , and 90  $\mu\text{m}$ , (10) reference catalog for the IR data for 9  $\mu\text{m}$ , 18  $\mu\text{m}$ , and 90  $\mu\text{m}$ , (11) hard X-ray flux in the 14–195 keV band, (12) hard X-ray luminosity in the 14–195 keV band ( $L_{\text{HX}}$ ), (13) X-ray absorption

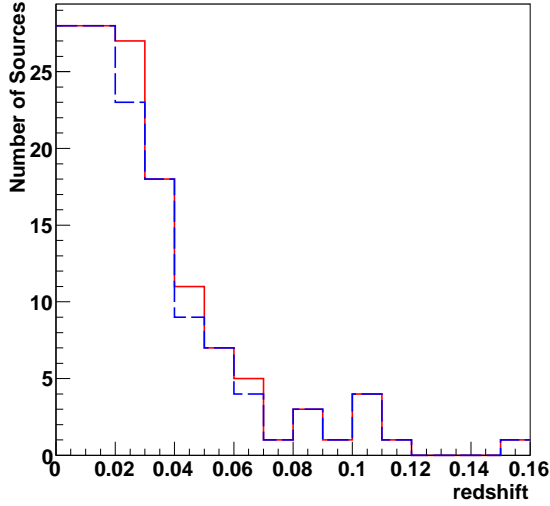


FIG. 3.— Redshift distribution of the whole non-blazar AGNs in the Swift/BAT 9-month catalog (red solid line: 135 objects) and of those with the MIR counterparts (blue dashed line: 128 objects).

column density ( $N_{\text{H}}$ ), (14) covering fraction in the X-ray spectrum ( $f_c$ ), and (15) the reference for the X-ray spectra. For AGNs whose AKARI MIR fluxes are not available, we convert the infrared fluxes and luminosities with IRAS or WISE into those at  $9 \mu\text{m}$  or  $18 \mu\text{m}$  according to the formula given in Section 2.5. Columns (1), (2), (3), (11) are taken from Tueller et al. (2008)<sup>4</sup>. The X-ray spectral information (columns 13–14) is basically adopted from Winter et al. (2009a), while we refer to the results obtained with *Suzaku* (Eguchi et al. 2009, 2011; Risaliti et al. 2009; Turner et al. 2009; Awaki et al. 2008; González-Martín et al. 2011; Winter et al. 2009b; Itoh et al. 2008; Tazaki et al. 2011; Winter & Mushotzky 2010; Bianchi et al. 2009) and those with *XMM-Newton* (Noguchi et al. 2010; Ballantyne 2005) whenever available. When the information is not available in Winter et al. (2009a), we refer to Tueller et al. (2008). All luminosities in this table are calculated by using the redshift given in column (3). There are total 13 new type AGNs out of the 135 AGNs, for which asterisks are attached to the source No. in Table 1 (column 1).

Figure 4 plots the hard X-ray luminosity distribution of our AGN sample with the MIR counterparts. Those for type-1 (dashed blue), type-2 (dotted red), and new-type (dot-dashed green) are separately plotted. Previous studies on Swift/BAT selected AGNs (Winter et al. 2009a; Burlon et al. 2011) have shown that the X-ray luminosity distribution of type-1 AGNs has a higher peak luminosity than that of type-2 ones, as expected from the well-known correlation that the fraction of absorbed AGNs decreases against luminosity (e.g., Ueda et al. 2003). Although such trend may not be clear in Figure 4 due to the smaller sample size and coarse bin width (0.5 dex), the averaged logarithmic luminosity of the type-1

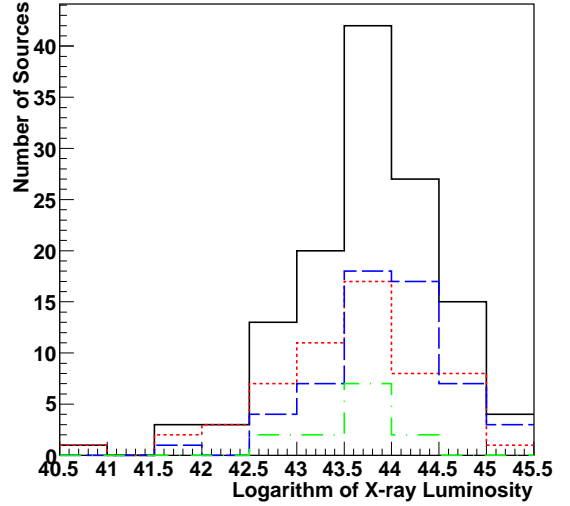


FIG. 4.— Distribution of the hard X-ray (14–195 keV) luminosity of our sample with MIR counterparts (total: black). The dashed blue, dotted red, and dot-dashed green ones correspond to those of the type-1, type-2, and new type AGNs, respectively.

and type-2 AGNs in our sample is 43.9 and 43.6, respectively, and a K-S test applied to their distributions returns a null probability of  $4.0 \times 10^{-2}$ . Thus, albeit marginal, type-1 AGNs are more luminous on average than type-2 AGNs in our sample.

### 3. RESULTS AND DISCUSSION

#### 3.1. Correlation between the Infrared and Hard X-ray Luminosities

Figure 5 shows the luminosity correlations in the luminosity range from  $10^{41} \text{ erg s}^{-1}$  to  $10^{46} \text{ erg s}^{-1}$  between the infrared (9, 18, or  $90 \mu\text{m}$ ) and *Swift*/BAT hard X-ray bands. Type-1, type-2, and new type AGNs are marked with squares (blue), circles (red), and diamonds (green), respectively. The small-filled symbols denote the data from AKARI, large-filled ones those from IRAS, and small-open ones those from WISE. In the figure, NGC 4395 is not shown due to its low luminosities ( $\log \lambda L_{\lambda}(9 \mu\text{m}), \log \lambda L_{\lambda}(18 \mu\text{m}), \log L_{\text{HX}} = (39.98, 40.28, 40.81)$ ). As noticed from the figure, the MIR (both 9 and  $18 \mu\text{m}$ ) luminosities well correlate with hard X-ray luminosity over 3 orders of magnitude (from  $10^{42} - 10^{45} \text{ erg s}^{-1}$ ). In the FIR ( $90 \mu\text{m}$ ) band, by contrast, the correlation is much weaker with larger dispersion compared with the MIR bands, even though we plot here only for AGNs detected with AKARI at  $90 \mu\text{m}$ .

Least-square fits to the hard X-ray versus MIR luminosity plots with a power law model (i.e., a linear function for the logarithmic luminosities with the form of  $\log(L_{\text{HX}}/10^{43}) = a + b \log(\lambda L_{\lambda}(9, 18 \mu\text{m})/10^{43})$ ) give the following best-fit correlations:

$$\log \frac{L_{\text{HX}}}{10^{43}} = (0.06 \pm 0.07) + (1.12 \pm 0.08) \log \frac{\lambda L_{\lambda}(9 \mu\text{m})}{10^{43}} \quad (5)$$

$$\log \frac{L_{\text{HX}}}{10^{43}} = (0.02 \pm 0.07) + (1.10 \pm 0.07) \log \frac{\lambda L_{\lambda}(18 \mu\text{m})}{10^{43}} \quad (6)$$

<sup>4</sup> The redshifts of two AGNs, No. 13: 2MASX J02162987+5126246 and No. 53: 2MASX J06403799-4321211, are adopted from <http://heasarc.gsfc.nasa.gov/docs/swift/results/bs58mon/>

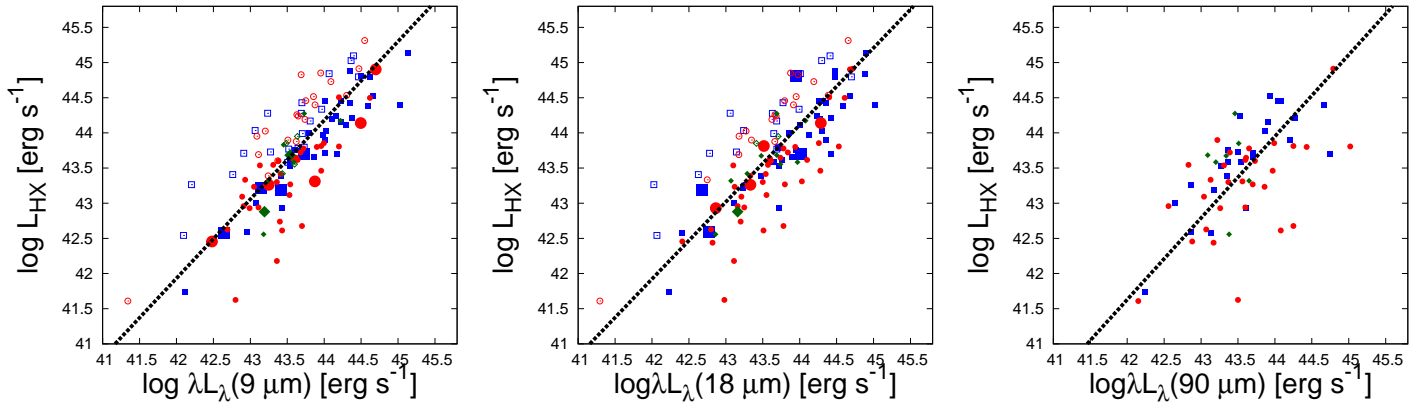


FIG. 5.— Correlation between the infrared (9  $\mu\text{m}$ , 18  $\mu\text{m}$ , or 90  $\mu\text{m}$ ) and hard X-ray (14–195 keV) luminosities. Squares (blue) represent type-1 AGNs ( $N_{\text{H}} < 10^{22}\text{cm}^{-2}$ ), circles (red) type-2 AGNs ( $N_{\text{H}} \geq 10^{22}\text{cm}^{-2}$ ), and diamonds (green) new type AGNs. Dotted lines represent the regression lines (see Section 3.1). The small-filled, large-filled, small-open symbols denote those with the AKARI, IRAS, and WISE counterparts, respectively. The IRAS and WISE fluxes are all converted into the 9  $\mu\text{m}$  (left) or 18  $\mu\text{m}$  (right) using the formula given in Section 2.5.

To check the significance of the correlations between the hard X-ray and MIR/FIR luminosities (or fluxes), we perform Spearman’s tests for the summed sample consisting of all AGN types. The results are summarized in Table 2, which has the following columns: Col. (1) sample; Col. (2) number of objects; Col. (3) luminosity-luminosity correlation coefficient ( $\rho_L$ ); Col. (4) flux-flux correlation coefficient ( $\rho_f$ ); Col. (5) a standard Student’s  $t$ -test null significance level for luminosity-luminosity correlations ( $P_L$ ); Col. (6) a standard Student’s  $t$ -test null significance level for flux-flux correlations ( $P_f$ ); Col. (7) regression intercept (a) and its 1- $\sigma$  uncertainty; Col. (8) regression slope (b) and its 1- $\sigma$  uncertainty. We find that both luminosity-luminosity and flux-flux correlations between the hard X-ray and MIR bands are highly significant. While there is also a significant correlation between 90  $\mu\text{m}$  and hard X-ray luminosity,  $(\rho_L, P_L) = (0.59, 4.5 \times 10^{-7})$ , their flux-flux correlation is weak with  $(\rho_f, P_f) = (0.17, 0.18)$ .

We establish the good correlation between the MIR and hard X-ray luminosities in AGNs from so far the largest, uniform AGN sample in the local universe, although similar results have been reported by several authors (Mushotzky et al. 2008; Gandhi et al. 2009; Vasudevan et al. 2010). The MIR emission from galaxies hosting an AGN is believed to originate mainly from high temperature ( $\sim 150$ – $300$  K) dust emission heated by X-ray/UV photons from the central engine. Thus, if extinction is not important, the MIR luminosity is expected to be correlated with the intrinsic X-ray luminosity, the most reliable tracers of the AGN power (since our sample contains mostly Compton thin AGNs with  $N_{\text{H}} < 10^{24}\text{cm}^{-2}$ , the observed 14–195 keV luminosity can be regarded as the intrinsic one without any correction). On the other hand, the FIR emission comes both from cooler ( $\sim 30$  K) interstellar dust heated by stars in host galaxies and from the cooler (outer) part of the torus in the AGN. The contribution from the host galaxy increases the scatter of the observed luminosity correlation, depending on the total star forming rate over the whole galaxy. Our results demonstrate that the MIR emission is more suitable for estimating the AGN intrinsic power than in the FIR band.

Figures 6 plot the histograms of the MIR to hard X-ray luminosity ratio in the logarithm scale ( $r \equiv \log \lambda L_{\lambda}(9\text{ }\mu\text{m})/L_{\text{HX}}$  and  $\log \lambda L_{\lambda}(18\text{ }\mu\text{m})/L_{\text{HX}}$ ) for the Swift/BAT AGN sample with MIR counterparts in the 9  $\mu\text{m}$  and 18  $\mu\text{m}$  bands, respectively, calculated from (a, d) total, (b, e) type-1 AGNs, and (c, f) type-2 + new type AGNs. Following Gandhi et al. (2009), we calculate its average and standard deviation for each sample, which are summarized in Table 3. From the total AGNs, we obtain  $(\bar{r}, \sigma) = (-0.129 \pm 0.039, 0.437 \pm 0.055)$  for the 9  $\mu\text{m}$  band and  $(\bar{r}, \sigma) = (-0.080 \pm 0.042, 0.473 \pm 0.059)$  for the 18  $\mu\text{m}$  band. We find that the average is consistent between type-1 and type-2 (plus new type) AGNs within the errors.

For comparison, the histogram of  $\log \lambda L_{\lambda}(12.3\text{ }\mu\text{m})/L_{\text{HX}}$  obtained by Gandhi et al. (2009) from 42 local AGNs are overplotted in Figures 6(a) and (d), where we convert their 2–10 keV luminosities into the 14–195 keV band by assuming a power law photon index of 2. Their sample is selected from nearby AGNs with good available X-ray spectra observed with *Suzaku*, *INTEGRAL*, or *Swift*, whose average distance is 74 Mpc (or  $z = 0.017$ ), consisting of 12 Seyfert 1s, 19 Seyfert 2s, 3 LINERs, and 8 Compton thick ( $N_{\text{H}} \geq 1.5 \times 10^{24}\text{cm}^{-2}$ ) AGNs. It is not a statistically complete sample, however. The average X-ray luminosity is  $\sim 42.9$  and only 3 sources have QSO class luminosity ( $L(2-10\text{ keV}) > 10^{44}\text{erg s}^{-1}$ ). Twenty four objects out of the 42 AGNs are listed in the Swift/BAT 9-month catalog and in our Table 1. We obtain  $(\bar{r}, \sigma) = (0.086 \pm 0.054, 0.353 \pm 0.077)$  for the 12.3  $\mu\text{m}$  band from the Gandhi et al. (2009) sample. Although the average is slightly larger than ours, it is still consistent within the error in the 18  $\mu\text{m}$  band. Note that silicate features (see below) may affect our result in the 9  $\mu\text{m}$  band. The standard deviation is almost the same between the Gandhi et al. (2009) sample and ours; the small difference could be due to the fact that there are 22 “well-resolved” AGNs in Gandhi et al. (2009), whose nucleus MIR emission was spatially separated from the host galaxy, making the correlation between the MIR and X-ray luminosities tighter.

We also check the consistency with the results by

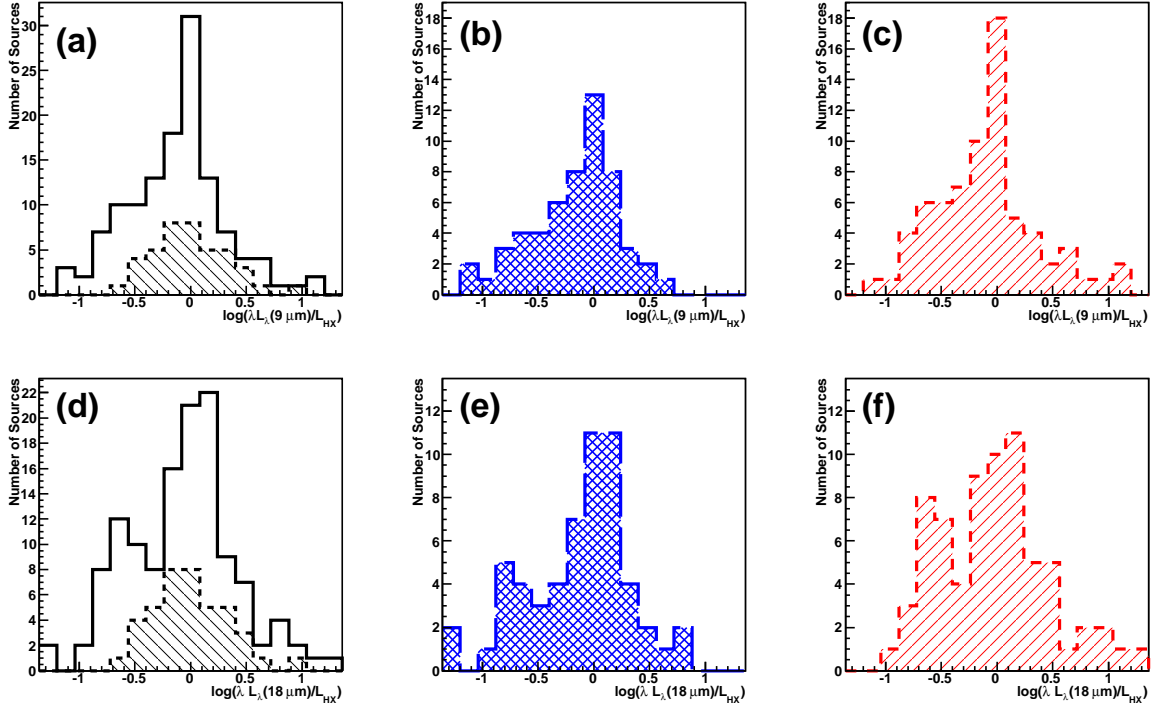


FIG. 6.— Histograms of  $\log(\lambda L_\lambda(9 \mu\text{m})/L_{\text{HX}})$  (top) and  $\log(\lambda L_\lambda(18 \mu\text{m})/L_{\text{HX}})$  (bottom). (a) and (d) (left): total AGNs (solid lines), (b) and (e) (center): type-1 AGNs, (c) and (f) (right): type-2 + new type AGNs. That of  $\log(\lambda L_\lambda(12.3 \mu\text{m})/L_{\text{HX}})$  for the Gandhi et al. (2009) sample is overplotted in panel (a) and (d) (dashed lines, hatched area).

Matsuta et al. (2012) obtained from the cross correlation between the Swift/BAT 22 month sample and the AKARI catalog. We confirm that our best-fit slopes ( $b$ ) of the linear correlations between  $\log \lambda L_\lambda(9, 18 \mu\text{m})$  and  $\log L_{\text{HX}}$  are well consistent with their results (1.13 for  $9 \mu\text{m}$  and 1.12 for  $18 \mu\text{m}$  with average errors of 0.04). On the other hand, the averaged MIR to X-ray luminosity ratios ( $\bar{r}$ ) derived from our study are slightly smaller than those by Matsuta et al. (2012) (0.14 for  $9 \mu\text{m}$  and 0.19 for  $18 \mu\text{m}$ ). The difference is attributable to the high completeness of identification in our analysis, where faint, WISE-only detected MIR sources are included.

As noticed from Figure 5, all types of AGNs (type-1, type-2, and new type) seem to follow almost the same MIR vs hard X-ray luminosity correlation. In fact, we see no significant difference in the distribution of their luminosity ratio between type-1 and type-2/new type AGNs (Table 3). To check this further, we plot  $\lambda L_\lambda(9 \mu\text{m})/L_{\text{HX}}$  and  $\lambda L_\lambda(18 \mu\text{m})/L_{\text{HX}}$  as a function of the absorption column density ( $N_{\text{H}}$ ) in Figure 7. In both panels, there is no clear dependence of the MIR to X-ray luminosity ratio on  $N_{\text{H}}$  up to  $\log N_{\text{H}} \simeq 24$ . The large ratios found for Compton thick AGNs can be partially explained by attenuation of the hard X-ray fluxes due to heavy obscuration. The absence of  $N_{\text{H}}$  dependence suggests that the emission from the AGN-heated dust seems not to be affected by the obscuration by the torus causing the X-ray absorption. The results cannot be explained with homogeneous dust torus models (Pier & Krolik 1992, 1993), which predict the significant decrease in the MIR to X-ray luminosity ratio when an optically-thick line-of-sight through the torus primarily show cooler smooth-dust and a lower mid-infrared luminosity for the same X-ray lu-

minosity than does an optically-thin one. Our results rather favor the clumpy dust tori model (Hönig et al. 2006; Nenkova et al. 2008a; Schartmann et al. 2008), which predicts isotropic MIR emission, as discussed in Gandhi et al. (2009). No clear difference is seen in the MIR to X-ray luminosity correlation between normal AGNs and new type AGNs. New type AGNs may have large intrinsic MIR luminosities because of the geometrically thick torus (Nenkova et al. 2008b), which could be partially canceled out due to extinction, however. Currently, the possible contribution from the host galaxy in the MIR band makes direct comparison between individual objects very difficult. We need more observations of these AGNs by resolving only the nucleus emission as done in Gandhi et al. (2009).

Meléndez et al. (2008a,b); Weaver et al. (2010) proposed the [Ne V]  $14.32/24.32 \mu\text{m}$  and [O IV]  $25.89 \mu\text{m}$  lines as good AGN indicators because of their high ionization potential. Using a Swift/BAT sample, Weaver et al. (2010) found a tight luminosity correlation between these lines and hard X-ray luminosities with a scatter of  $\sim 0.5$  dex, which is almost comparable with our result obtained for the MIR and hard X-ray correlation ( $\approx 0.45$  dex, see Table 2). The correlation we find is very useful and easy to apply to various survey data as it requires only photometry without spectroscopy.

### 3.2. Averaged IR Spectral Energy Distribution

Spectra in the MIR band are quite useful to investigate the host galaxy properties of AGNs. It is known that Polycyclic Aromatic Hydrocarbon (PAH) features in the  $3 \mu\text{m}$  to  $20 \mu\text{m}$  band (Tielens 2008) can be used as a starburst tracer (Imanishi & Dudley 2000). The



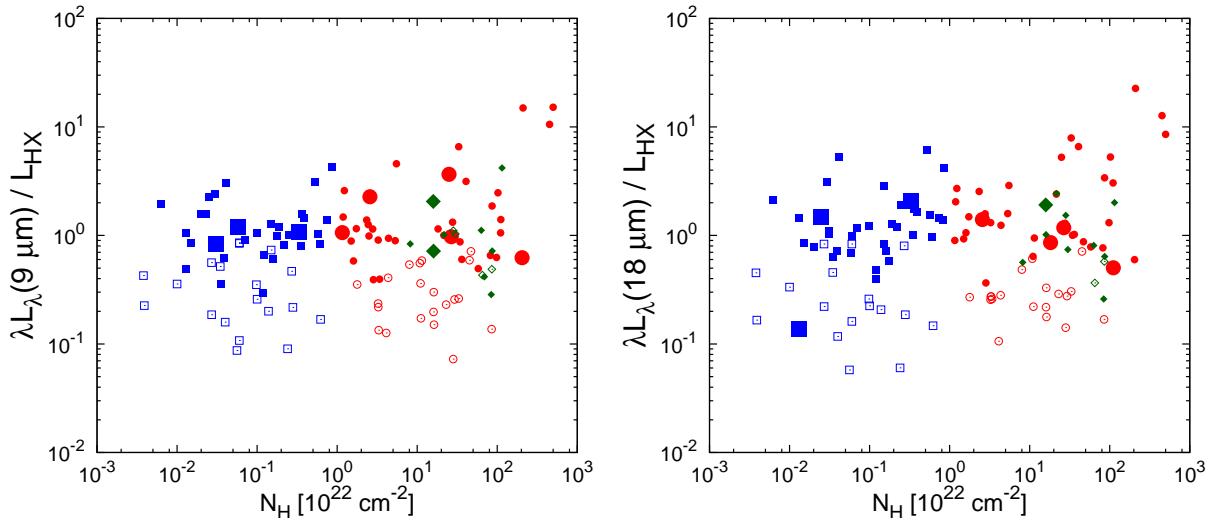


FIG. 7.— The MIR to hard X-ray luminosity ratio plotted against the absorption column density. Left:  $\lambda L_{\lambda}(9 \mu\text{m})/L_{\text{HX}}$ . Right:  $\lambda L_{\lambda}(18 \mu\text{m})/L_{\text{HX}}$ . All symbols are the same as Figure 5.

AKARI 9  $\mu\text{m}$  band covers the strong PAH emission feature at 7.7, 8.6, and 11.2  $\mu\text{m}$ . In addition, opacity peak of amorphous silicate grains are located around 10 and 18  $\mu\text{m}$  due to the Si–O stretching and the O–Si–Y bending modes. Hao et al. (2007) report the MIR spectra of different types of AGNs (type-1 QSO, type-1 Seyfert, type-2 Seyfert, ULIRG) from Spitzer observations, revealing a large variety in the 10  $\mu\text{m}$  silicate feature. Silicate absorption feature is clearly detected from type-2 Seyferts.

Averaged SEDs in the NIR to FIR band of the three types of AGNs are presented in Figure 8. The spectrum of each AGN is normalized by the 18  $\mu\text{m}$  luminosity. Here we only use total 42 sources detected in all the 9, 18, and 90  $\mu\text{m}$  bands, consisting of 16 type-1, 21 type-2, and 5 new type AGNs. We also include the photometric data in the  $J$ ,  $H$ , and  $K_s$  bands adopted from the 2 Micron All Sky Survey (2MASS) Point Source Catalog. We neglect the effect of redshift because the sample consists of only local AGNs ( $z < 0.1$  with a mean value of  $\langle z \rangle = 0.0165$ ), for which K-correction is not significant.

We find that the FIR emission at 90  $\mu\text{m}$  is weaker relative to 18  $\mu\text{m}$  in the type-1 AGNs (blue) than in type-2 (red) and new type AGNs (green). On the other hand, the MIR spectra are almost the same between the type-1 and type-2 AGNs. This can be explained because type-1 AGNs have intrinsically higher AGN luminosities on average than type-2 AGNs (see Figure 4), and hence contribution from cool dust in the host galaxy emitting the FIR radiation becomes smaller relative to the AGN component mainly observed in the MIR band. Indeed, the same trend is seen in the observed SED templates of Seyfert 2 galaxies and type-1 QSOs compiled by Polletta et al. (2007) (see their Figure 1). Another possible explanation would be an intrinsic difference of the dust quantity between type-1 and type-2 AGNs: Malkan et al. (1998) suggested that the host galaxies of type-2 AGNs are likely to be more dusty than those of type-1 AGNs from the results of a Hubble Space Telescope imaging survey of nearby AGNs.

It is remarkable that the averaged SED of new type AGNs exhibit enhanced fluxes than type-2 AGNs at 9

$\mu\text{m}$ . In fact, this is confirmed in the individual SED for 4 objects (ESO 005-G004, ESO 506-G027, NGC 7172 and NGC 7319) out of the 5 new type AGNs examined here. This 9  $\mu\text{m}$  excess most probably attributable to the PAH emission feature at 7.7, 8.6, and 11.2  $\mu\text{m}$  from the host galaxies. This is consistent with the larger 90  $\mu\text{m}$  excess in the averaged new-type AGN spectrum than in type-2 AGNs, which also reflects the starburst activity in the host galaxies. Another possibility is that the 9  $\mu\text{m}$  excess comes from the emission feature of silicate grains, which would imply a larger amount of dusts around the nucleus than in normal type-2 AGNs. Our result suggests that geometrically thick tori around the black hole may form in galaxies with high star forming rates.

Four out of the 5 new type AGNs have available MIR spectra observed with *Spitzer*. ESO 005-G004 shows a clear 11.2  $\mu\text{m}$  PAH line, and silicate absorption features are suggested at  $\lambda > 10 \mu\text{m}$  (Weaver et al. 2010). A detection of the 11.2  $\mu\text{m}$  PAH line is reported from ESO 506-G027 (Sargsyan et al. 2011), although the spectrum is not available in the literature. NGC 7172 shows PAH lines at 7.7  $\mu\text{m}$  and 11.2  $\mu\text{m}$  with strong silicate absorption features. In addition, for ESO 005-G004 and NGC 7172, the line flux ratio between [Ne III] 15.56  $\mu\text{m}$  and [Ne II] 12.81  $\mu\text{m}$  is available in Weaver et al. (2010), from which the relative strength of the starburst to AGN activities can be estimated. These two sources have  $\log f_{[\text{NeIII}]} / f_{[\text{NeII}]} = -0.50$  and  $-0.31$ , respectively, suggesting that both have relatively strong starburst components normalized by their AGN activities. Thus, though limited in sample, a majority of our new type AGNs indeed show significant PAH emission lines (and silicate absorption features) contributing to the 9  $\mu\text{m}$  excess. Further systematic investigation of the MIR spectra of hard X-ray selected AGNs is useful to reveal the host galaxy properties and environment around the central engine in relation to the X-ray spectral information.

#### 4. SUMMARY AND CONCLUSIONS

We have systematically studied the MIR and FIR properties of a large complete flux limited AGN sample in the



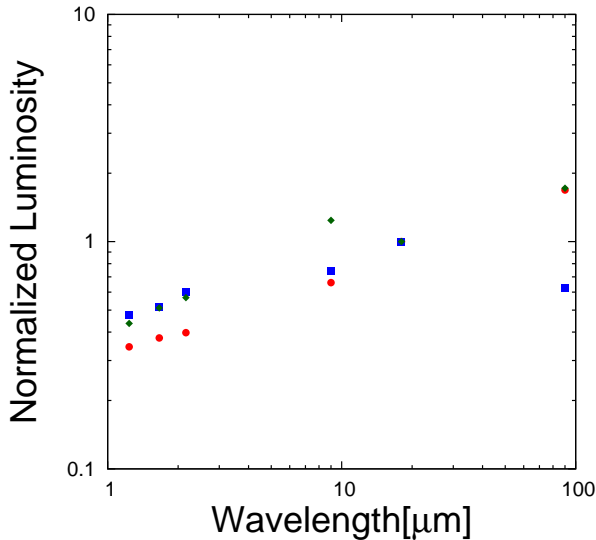


FIG. 8.— Averaged infrared (1–100  $\mu\text{m}$ ) SED normalized at the 18  $\mu\text{m}$  band for type-1 (blue, filled square), type-2 (red, filled circle), and new type AGNs (green, diamond).

local universe detected in the Swift/BAT all sky survey in the 14–195 keV band, which has the least bias against obscuration. Utilizing the AKARI, IRAS, and WISE infrared catalogs, we unambiguously identify 128 counterparts in the MIR band out of the 135 non-blazar AGNs in the Swift/BAT 9-month catalog by Tueller et al. (2008). For our discussion, the whole sample is divided into 3 types based on the X-ray spectra, 57 type-1, 58 type-2, and 13 “new type” AGNs showing extremely small scattered fractions.

The two main conclusions are summarized as follows:

1. We find a good luminosity correlation between the MIR (9  $\mu\text{m}$  and 18  $\mu\text{m}$ ) and hard X-ray band over three orders of magnitude ( $42 < \log L_{\text{HX}} < 45$ ), while that between the FIR (90  $\mu\text{m}$ ) and hard X-ray bands is weaker, most probably due to the

larger contribution from the host galaxy (Figure 5). All types of AGNs follow the same correlation, and the luminosity ratio between the MIR to X-ray bands show no clear dependence against absorption column density up to  $N_{\text{H}} \sim 10^{24} \text{ cm}^{-2}$ . Our results favor isotropic infrared emission models, possibly clumpy dust torus models rather than homogeneous dust model, confirming the argument by Gandhi et al. (2009) but with a much larger sample.

2. We find 9  $\mu\text{m}$  excess in the averaged infrared SED of “new type” AGNs. This could be attributable to the PAH emission features, as confirmed in the available *Spitzer* spectra of at least three sources, suggesting that their host galaxies have strong star-burst activities.

This research is based on observations with AKARI, a JAXA project with the participation of ESA, and those with Wide-field Infrared Survey Explorer, which is a joint project of the University of California, Los Angeles, and the Jet Propulsion Laboratory/California Institute of Technology, funded by the National Aeronautics and Space Administration. The publication makes use of the NASA/ IPAC Infrared Science Archive, which is operated by the Jet Propulsion Laboratory, California Institute of Technology, under contract with the National Aeronautics and Space Administration. This work is partly supported by the Grant-in-Aid for Scientific Research 23540265 (YU) and 21244017 (YT), and by the grant-in-aid for the Global COE Program “The Next Generation of Physics, Spun from Universality and Emergence” from the Ministry of Education, Culture, Sports, Science and Technology (MEXT) of Japan.

## REFERENCES

- Awaki, H., Anabuki, N., Fukazawa, Y., et al. 2008, PASJ, 60, 293  
 Ballantyne, D. R. 2005, MNRAS, 362, 1183  
 Beichman, C. A., Neugebauer, G., Habing, H. J., Clegg, P. E., & Chester, T. J. 1988, Infrared astronomical satellite (IRAS) catalogs and atlases. Volume 1: Explanatory supplement, 1,  
 Bianchi, S., Piconcelli, E., Chiaberge, M., et al. 2009, ApJ, 695, 781  
 Bird, A. J., Bazzano, A., Bassani, L., et al. 2010, ApJS, 186, 1  
 Brandt, W. N., & Hasinger, G. 2005, ARA&A, 43, 827  
 Burlon, D., Ajello, M., Greiner, J., et al. 2011, ApJ, 728, 58  
 Comastri, A., Iwasawa, K., Gilli, R., Vignali, C., Ranalli, P., Matt, G., & Fiore, F. 2010, ApJ, 717, 787  
 Eguchi, S., Ueda, Y., Terashima, Y., Mushotzky, R., & Tueller, J. 2009, ApJ, 696, 1657  
 Eguchi, S., Ueda, Y., Awaki, H., Aird, J., Terashima, Y., & Mushotzky, R. 2011, ApJ, 729, 31  
 Gallimore, J. F., Yzaguirre, A., Jakoboski, J., Stevenosky, M. J., Axon, D. J., Baum, S. A., Buchanan, C. L., Elitzur, M., Elvis, M., O’Dea, C. P., & Robinson, A. 2010 ApJS, 187, 172  
 Gandhi, P., Horst, H., Smette, A., Hönig, S., Comastri, A., Gilli, R., Vignali, C., & Duschl, W. 2009, A&A, 502, 457  
 González-Martín, O., Papadakis, I., Braitto, V., et al. 2011, A&A, 527, A142  
 Hao, L., Weedman, D. W., Spoon, H. W. W., Marshall, J. A., Levenson, N. A., Elitzur, M., & Houck, J. R. 2007, ApJ, 655, L77  
 Hasinger, G., Miyaji, T., & Schmidt, M. 2005, A&A, 441, 417  
 Hönig, S. F., Beckert, T., Ohnaka, K., & Weigelt, G. 2006, A&A, 452, 459  
 Horst, H., Gandhi, P., Smette, A., & Duschl, W. J. 2008, A&A, 479, 389  
 Hopkins, P. F., Hernquist, L., Cox, T. J., Di Matteo, T., Martini, P., Robertson, B., & Springel, V. 2005, ApJ, 630, 705  
 Imanishi, M., & Dudley, C. C. 2000, ApJ, 545, 70  
 Ishihara, D., Onaka, T., Kataza, H., et al. 2010, A&A, 514, A1  
 Itoh, T., Done, C., Makishima, K., et al. 2008, PASJ, 60, 251  
 Kawada, M., Baba, H., Barthel, P. D., et al. 2007, PASJ, 59, 389  
 Lamastra, A., Perola, G. C., & Matt, G. 2006, A&A, 449, 551  
 Malkan, M. A., Gorjian, V., & Tam, R. 1998, ApJS, 117, 25  
 Matsuta, K., Gandhi, P., Dotani, T., Nakagawa, T., et al. 2012, ApJ accepted  
 Meléndez, M., Kraemer, S. B., Armentrout, B. K., et al. 2008, ApJ, 682, 94  
 Meléndez, M., Kraemer, S. B., Schmitt, H. R., et al. 2008, ApJ, 689, 95  
 Murakami, H., Baba, H., Barthel, P., et al. 2007, PASJ, 59, 369  
 Murayama, T., Mouri, H., & Taniguchi, Y. 2000, ApJ, 528, 179  
 Mushotzky, R. F., Winter, L. M., McIntosh, D. H., & Tueller, J. 2008, ApJ, 684, L65  
 Nenkova, M., Sirocky, M. M., Ivezić, Ž., & Elitzur, M. 2008, ApJ, 685, 147  
 Nenkova, M., Sirocky, M. M., Nikutta, R., Ivezić, Ž., & Elitzur, M. 2008 ApJ, 685, 160

- Neugebauer, G., Habing, H. J., van Duinen, R., et al. 1984, *ApJ*, 278, L1
- Noguchi, K., Terashima, Y., Ishino, Y., et al. 2010, *ApJ*, 711, 144
- Onaka, T., Matsuhara, H., Wada, T., et al. 2007, *PASJ*, 59, 401
- Oyabu, S., Ishihara, D., Malkan, M., et al. 2011, *A&A*, 529, A122
- Pier, Edward A., & Krolik, Julian H. 1992, *ApJ*, 705, 454
- Pier, Edward A., & Krolik, Julian H. 1993, *ApJ*, 418, 673
- Polletta, M., Tajer, M., Maraschi, L., et al. 2007, *ApJ*, 663, 81
- Risaliti, G., Braito, V., Laparola, V., et al. 2009, *ApJ*, 705, L1
- Sargsyan, L., Weedman, D., Lebouteiller, V., et al. 2011, *ApJ*, 730, 19
- Schartmann, M., Meisenheimer, K., Camenzind, M., et al. 2008, *A&A*, 482, 67
- Tazaki, F., Ueda, Y., Ishino, Y., et al. 2010, *ApJ*, 721, 1340
- Tazaki, F., Ueda, Y., Terashima, Y., & Mushotzky, R. F. 2011, *ApJ*, 738, 70
- Tielens, A. G. G. M. 2008, *ARA&A*, 46, 28
- Tueller, J., Mushotzky, R. F., Barthelmy, S., Cannizzo, J. K., Gehrels, N., Markwardt, C. B., Skinner, G. K., & Winter, L. M. 2008, *ApJ*, 681, 113
- Tueller, J., et al. 2010, *ApJS*, 186, 378
- Turner, T. J., Miller, L., Kraemer, S. B., Reeves, J. N., & Pounds, K. A. 2009, *ApJ*, 698, 99
- Ueda, Y., Akiyama, M., Ohta, K., & Miyaji, T. 2003, *ApJ*, 598, 886
- Ueda, Y., Eguchi, S., Terashima, Y., et al. 2007, *ApJ*, 664, L79
- Vasudevan, R. V., Fabian, A. C., Gandhi, P., Winter, L. M., & Mushotzky, R. F. 2010, *MNRAS*, 402, 1081
- Weaver, K. A., Meléndez, M., Mushotzky, R. F., Kraemer, S., Engle, K., Malumuth, E., Tueller, J., Markwardt, C., Berghea, C. T., Dudik, R. P., Winter, L. M., & Armus, L. 2010, *ApJ*, 716, 1151
- Winkler, C., Courvoisier, T. J.-L., Di Cocco, G., et al. 2003, *A&A*, 411, L1
- Winter, Lisa M., Mushotzky, Richard F., Reynolds, Christopher S., & Tueller, Jack. 2009, *ApJ*, 690, 1322
- Winter, Lisa M., Mushotzky, Richard F., Terashima, Yuichi., & Ueda, Yoshihiro. 2009, *ApJ*, 701, 1644
- Winter, L. M., & Mushotzky, R. 2010, *ApJ*, 719, 737
- Wright, E. L., Eisenhardt, P. R. M., Mainzer, A. K., et al. 2010, *AJ*, 140, 1868
- Yamamura, I., Makiuti, S., Ikeda, N., Fukuda, Y., Oyabu, S., Koga, T., & White, G. J. 2010, *VizieR Online Data Catalog*, 2298, 0

TABLE 1  
INFRARED AND X-RAY PROPERTIES OF THE AGNs IN THE 9-MONTH  
*Swift*/BAT CATALOG

No.	Object	$z$	$f(9)$	$f(18)$	$f(90)$	$\lambda L_{\lambda}(9)$	$\lambda L_{\lambda}(18)$	$\lambda L_{\lambda}(90)$	IR Catalog	$f_{\text{HX}}$	$\log L_{\text{HX}}$	$N_{\text{H}}$	$f_c$	X-ray Catalog
(1)	(2)	(3)	(4)	(5)	(6)	(7)	(8)	(9)	(10)	(11)	(12)	(13)	(14)	(15)
1**	NGC 235A	0.022229	0.136	0.295	...	43.60	43.74	...	(W, A, X)	3.2	43.56	28.2	0.9975	(a)
2**	Mrk 348	0.015034	0.308	0.593	0.736	43.54	43.69	43.09	(I, A, A)	9.5	43.68	16.0	0.9960	(c)
3	Mrk 352	0.014864	0.012	0.016	...	42.20	42.02	...	(W, W, X)	3.7	43.26	0.056	...	(b)
4**	NGC 454	0.012125	0.213	0.417	...	43.19	43.16	...	(I, I, X)	2.3	42.88	15.9	0.9970	(a)
5	Fairall 9	0.04702	0.229	0.440	...	44.59	44.58	...	(A, A, X)	4.7	44.39	0.023	...	(b)
6	NGC 526A	0.019097	0.141	0.292	...	43.58	43.60	...	(A, A, X)	5.2	43.63	1.50	...	(a)
7	NGC 612	0.029771	0.135	0.153	2.604	43.96	43.52	44.25	(A, I, A)	3.2	43.81	111	0.9945	(a)
8**	ESO 297-G018	0.025201	0.081	0.132	0.672	43.49	43.41	43.51	(W, W, A)	4.9	43.85	65.1	0.9972	(a)
9	NGC 788	0.013603	0.162	0.312	...	43.24	43.33	...	(W, A, X)	5.9	43.39	46.9	0.9930	(a)
10	Mrk 1018	0.04244	0.059	0.085	...	43.81	43.69	...	(W, W, X)	3.5	44.17	0	...	(a)
11	LEDA 138501	0.0492	...	...	...	...	...	...	(X, X, X)	3.9	44.35	0.030	...	(a)
12	Mrk 590	0.02638	0.080	0.227	...	43.52	43.69	...	(W, W, X)	3.7	43.77	0.027	...	(b)
13	2MASX J02162987+5126246	0.0288	...	...	...	...	...	...	(X, X, X)	3.6	43.84	1.74	...	(a)
15	NGC 931	0.016652	0.349	0.763	2.430	43.86	43.90	43.70	(A, A, A)	7.3	43.66	0.360	...	(a)
16	NGC 985	0.043	0.165	0.368	1.291	44.37	44.42	44.27	(A, A, A)	3.7	44.20	0.389	...	(b)
17	ESO 416-G002	0.059198	0.023	0.052	...	43.70	43.77	...	(W, W, X)	3.2	44.43	0.027	...	(b)
18	ESO 198-024	0.0455	0.039	0.064	...	43.69	43.63	...	(W, W, X)	3.9	44.28	0.100	...	(b)
19	QSO B0241+622	0.044	0.300	0.635	0.576	44.66	44.68	43.94	(A, A, A)	7.3	44.52	0.742	...	(a)
20**	NGC 1142	0.028847	0.265	0.380	...	44.22	44.08	...	(A, A, X)	7.8	44.17	63.1	0.9974	(e)
21	2MASX J03181899+6829322	0.0901	0.017	0.027	...	43.95	43.88	...	(W, W, X)	3.5	44.85	4.10	0.9670	(a)
22	NGC 1275	0.017559	0.442	1.988	6.928	44.01	44.36	44.21	(A, A, A)	11.5	43.90	0.151	...	(a)
23	PKS 0326-288	0.108	...	0.152	...	...	44.88	...	(X, A, X)	2.3	44.84	0.031	...	(a)
24	NGC 1365	0.005457	2.234	5.364	80.384	43.70	43.78	44.25	(A, A, A)	7.2	42.68	450	0.7400	(f)
25	ESO 548-G081	0.01448	0.248	0.097	0.968	43.42	42.68	43.18	(I, I, A)	3.3	43.19	0	...	(a)
27	PGC 13946	0.036492	0.015	0.036	...	43.09	43.18	...	(W, W, X)	2.9	43.95	85.0	0.9797	(e)
28	2MASX J03565655-4041453	0.0747	0.020	0.048	...	43.85	43.95	...	(W, W, X)	2.4	44.52	3.27	...	(a)
29	3C 105	0.089	0.009	0.035	...	43.69	43.98	...	(W, W, X)	3.4	44.83	28.2	0.9730	(a)
30	3C 111.0	0.0485	0.081	0.135	...	44.07	44.01	...	(W, W, X)	12.5	44.84	0.620	...	(a)
31	1H 0419-577	0.104	0.081	0.106	...	44.70	44.68	...	(I, A, X)	2.9	44.90	204	...	(g)
32	3C 120	0.03301	0.203	0.497	1.468	44.23	44.31	44.08	(A, A, A)	11.2	44.45	0.160	...	(a)
33	2MASX J04440903+2813003	0.01127	0.090	0.145	1.427	42.93	42.75	43.13	(A, W, A)	7.6	43.33	3.39	0.9900	(a)
34	MCG -01-13-025	0.015894	0.039	0.055	...	42.76	42.63	...	(W, W, X)	4.5	43.41	0.004	...	(b)
35	1RXS J045205.0+493248	0.029	...	...	...	...	...	...	(X, X, X)	5.6	44.03	0.001	...	(a)
36	XSS J05054-2348	0.035043	0.060	0.124	...	43.65	43.68	...	(W, W, X)	6.1	44.24	29.3	0.9914	(e)
37	4U 0517+17	0.017879	0.166	0.748	0.957	43.60	43.95	43.36	(A, A, A)	7.8	43.75	0	...	(a)
38	Ark 120	0.032296	0.252	0.253	...	44.30	44.00	...	(A, A, X)	5.3	44.11	0.020	...	(a)
39	ESO 362-G018	0.012642	0.224	0.570	...	43.25	43.33	...	(I, I, X)	5.1	43.26	26.6	0.9130	(a)
40	PICTOR A	0.035058	0.073	0.135	...	43.73	43.72	...	(W, W, X)	2.2	43.80	0.060	...	(a)
45	NGC 2110	0.007789	0.300	0.566	4.594	43.13	43.10	43.31	(A, A, A)	25.6	43.54	2.84	0.9520	(a)
46	MCG +08-11-011	0.020484	0.340	1.283	2.377	44.03	44.30	43.87	(A, A, A)	11.1	44.02	0.250	...	(a)
47	EXO 055620-3820.2	0.03387	0.532	0.691	...	44.50	44.29	...	(I, I, X)	5.2	44.14	2.57	0.9660	(a)
48	IRAS 05589+2828	0.033	0.201	0.454	0.955	44.23	44.28	43.90	(A, A, A)	5.6	44.15	0	...	(a)
49**	ESO 005-G004	0.006228	0.537	0.520	8.501	43.18	42.86	43.38	(A, A, A)	4.2	42.56	115	0.9973	(e)
50	Mrk 3	0.013509	0.322	1.892	2.939	43.64	44.10	43.60	(A, A, A)	10.1	43.62	110	...	(h)
51	ESO 121-IG028	0.0403	0.016	0.037	...	43.20	43.27	...	(W, W, X)	2.8	44.03	16.2	...	(a)
52	ESO 490-IG026	0.0248	0.173	0.706	...	43.73	44.02	...	(I, I, X)	3.6	43.70	0.330	...	(a)
53	2MASX J06403799-4321211	0.061	0.032	0.068	...	43.88	43.92	...	(W, W, X)	2.8	44.40	16.1	...	(a)
54	2MASX J06411806+3249313	0.047	0.042	0.089	...	43.75	43.80	...	(W, W, X)	5.5	44.46	16.0	...	(a)
55	Mrk 6	0.01881	0.180	0.522	0.920	43.68	43.84	43.39	(A, A, A)	6.6	43.72	3.26	0.9090	(a)
56	Mrk 79	0.022189	0.276	0.611	1.358	44.01	44.05	43.70	(A, A, A)	4.7	43.72	0.006	...	(b)

TABLE 1 — CONTINUED

No.	Object	$z$	$f(9)$	$f(18)$	$f(90)$	$\lambda L_{\lambda}(9)$	$\lambda L_{\lambda}(18)$	$\lambda L_{\lambda}(90)$	IR Catalog	$f_{\text{HX}}$	$\log L_{\text{HX}}$	$N_{\text{H}}$	$f_c$	X-ray Catalog
(1)	(2)	(3)	(4)	(5)	(6)	(7)	(8)	(9)	(10)	(11)	(12)	(13)	(14)	(15)
58	IGR J07597–3842	0.04	...	...	...	...	...	...	(X, X, X)	5.3	44.30	0	...	(a)
60	Mrk 18	0.011088	0.106	0.252	2.010	42.99	42.86	43.26	(A, I, A)	3.1	42.93	18.2	0.9700	(a)
61	2MASX J09043699+5536025	0.037	0.014	0.040	...	43.07	43.24	...	(W, W, X)	3.4	44.03	0.060	...	(a)
62	2MASX J09112999+4528060	0.026782	0.030	0.067	...	43.11	43.18	...	(W, W, X)	3.0	43.69	33.0	0.9940	(a)
63	IRAS 09149–6206	0.0573	0.407	0.792	1.735	45.03	45.02	44.66	(A, A, A)	3.2	44.40	0.850	...	(a)
64	2MASX J09180027+0425066	0.156	0.021	0.050	...	44.55	44.66	...	(W, W, X)	3.1	45.31	11.1	0.9870	(a)
65	MCG –01-24-012	0.019644	0.104	0.263	...	43.37	43.58	...	(W, A, X)	4.6	43.60	11.4	...	(a)
66	MCG +04-22-042	0.032349	0.078	0.178	...	43.79	43.85	...	(A, A, X)	4.1	44.00	0.039	...	(b)
67	Mrk 110	0.03529	0.073	0.107	...	43.74	43.62	...	(W, W, X)	5.4	44.19	1.78	...	(a)
68	NGC 2992	0.007709	0.299	0.826	9.220	43.11	43.25	43.60	(A, A, A)	6.6	42.94	1.19	0.4760	(a)
69	MCG –05-23-016	0.008486	0.384	1.391	1.277	43.31	43.57	42.83	(A, A, A)	21.9	43.54	1.60	...	(a)
70	NGC 3081	0.007956	0.167	0.699	2.364	42.89	43.21	43.04	(A, A, A)	8.8	43.09	98.0	0.9937	(d)
71	NGC 3227	0.003859	0.444	1.128	10.596	42.69	42.80	43.07	(A, A, A)	12.9	42.63	1.74	0.8520	(a)
72	NGC 3281	0.010674	0.415	1.509	6.011	43.54	43.80	43.70	(A, A, A)	7.3	43.27	86.3	0.9810	(a)
73	2MASX J10384520–4946531	0.06	...	...	...	...	...	...	(X, X, X)	3.3	44.45	1.81	0.8800	(a)
74	LEDA 093974	0.023923	0.096	0.256	0.941	43.62	43.74	43.61	(A, A, A)	3.4	43.65	4.38	0.9860	(a)
75**	Mrk 417	0.032756	0.068	0.152	...	43.64	43.71	...	(W, W, X)	3.6	43.95	85.7	0.9983	(a)
77	NGC 3516	0.008836	0.262	0.651	1.317	43.17	43.27	42.87	(A, A, A)	10.6	43.27	0.353	...	(a)
78	RX J1127.2+1909	0.1055	0.040	0.130	...	44.47	44.70	...	(W, W, X)	2.2	44.80	0.270	...	(a)
79	NGC 3783	0.00973	0.502	1.530	2.716	43.54	43.72	43.27	(A, A, A)	16.1	43.53	0.570	0.7220	(a)
80	SBS 1136+594	0.0601	0.041	0.083	...	43.97	43.99	...	(W, W, X)	2.5	44.34	0.004	...	(a)
81	UGC 06728	0.006518	0.051	0.091	...	42.10	42.07	...	(W, W, X)	3.7	42.54	0.010	...	(a)
82	2MASX J11454045–1827149	0.032949	0.078	0.131	...	43.70	43.65	...	(W, W, X)	3.9	43.99	0.035	...	(a)
83	CGCG 041–020	0.036045	0.054	0.112	...	43.62	43.66	...	(W, W, X)	2.5	43.88	10.8	0.9910	(a)
84	IGR J12026–5349	0.027966	0.166	0.614	1.630	44.00	44.26	43.99	(A, A, A)	4.0	43.86	2.34	...	(a)
85	NGC 4051	0.002335	0.346	0.885	4.557	42.12	42.23	42.24	(A, A, A)	4.6	41.74	0.029	...	(b)
86**	Ark 347	0.02244	0.091	0.102	...	43.43	43.29	...	(W, A, X)	2.3	43.42	30.0	0.9950	(a)
87	NGC 4102	0.002823	1.082	3.287	54.050	42.80	42.98	43.50	(A, A, A)	2.4	41.62	210	...	(i)
88	NGC 4138	0.002962	0.044	0.075	2.161	41.34	41.29	42.15	(W, W, A)	2.1	41.61	8.00	0.9880	(a)
89	NGC 4151	0.003319	1.032	3.629	4.594	42.91	43.16	42.56	(A, A, A)	37.4	42.96	5.32	0.9590	(a)
90	Mrk 766	0.012929	0.220	0.859	3.312	43.43	43.72	43.61	(A, A, A)	2.3	42.93	0.525	...	(b)
91	NGC 4388	0.008419	0.462	1.589	10.349	43.38	43.61	43.73	(A, A, A)	25.3	43.60	36.2	0.9920	(a)
92	NGC 4395	0.001064	0.013	0.052	...	39.94	40.25	...	(W, W, X)	2.6	40.81	3.30	0.6780	(a)
94	NGC 4507	0.011802	0.510	1.163	4.370	43.72	43.78	43.65	(A, A, A)	19.3	43.78	34.3	0.9710	(a)
95**	ESO 506-G027	0.025024	0.114	0.207	0.613	43.73	43.69	43.46	(A, A, A)	13.2	44.28	84.1	0.9981	(j)
96	XSS J12389–1614	0.036675	0.053	0.109	...	43.63	43.67	...	(W, W, X)	5.8	44.26	3.25	...	(a)
97	NGC 4593	0.009	0.344	0.569	...	43.14	43.23	...	(I, A, X)	9.1	43.21	0.031	...	(a)
98	WKK 1263	0.02443	0.091	0.170	0.769	43.51	43.58	43.54	(W, A, A)	2.8	43.58	0.060	...	(a)
100	SBS 1301+540	0.02988	0.015	0.022	...	42.91	42.78	...	(W, W, X)	2.5	43.71	0.040	...	(b)
101	NGC 4945	0.001878	8.811	9.945	...	43.36	43.11	...	(A, A, X)	19.4	42.18	500	...	(k)
102**	NGC 4992	0.025137	0.059	...	...	43.45	...	...	(A, X, X)	4.7	43.83	69.0	0.9974	(a)
103	MCG –03-34-064	0.016541	0.453	1.873	4.634	43.96	44.28	43.97	(A, A, A)	4.7	43.46	40.7	0.9610	(a)
104	Cen A	0.001825	10.190	13.150	...	43.40	43.20	...	(A, A, X)	74.8	42.74	5.50	...	(a)
105	MCG –06-30-015	0.007749	0.280	0.591	1.035	43.08	43.11	42.65	(A, A, A)	7.5	43.00	0.190	...	(a)
106	NGC 5252	0.022975	0.104	0.136	0.416	43.51	43.35	43.22	(W, W, A)	6.6	43.90	4.34	0.9620	(a)
107	4U 1344-60	0.012879	0.207	0.556	...	43.41	43.54	...	(A, A, X)	7.0	43.41	2.50	...	(a)
108	IC 4329A	0.016054	0.769	1.790	1.785	44.16	44.23	43.53	(A, A, A)	30.0	44.24	0.610	...	(a)
109	Mrk 279	0.030451	0.141	0.387	...	43.99	44.13	...	(A, A, X)	4.4	43.97	0.013	...	(a)
110	NGC 5506	0.006181	0.823	2.240	8.413	43.36	43.50	43.37	(A, A, A)	23.6	43.30	2.78	0.9893	(a)
112	NGC 5548	0.01717	0.157	0.409	1.073	43.54	43.65	43.37	(A, A, A)	5.8	43.59	0.070	...	(a)
113	ESO 511-G030	0.02239	0.064	0.090	0.847	43.27	43.14	43.50	(W, W, A)	4.7	43.73	0.098	...	(a)
115	NGC 5728	0.0093	0.176	0.418	11.383	43.05	43.12	43.86	(A, A, A)	8.9	43.23	82.0	...	(a)



TABLE 1 — CONTINUED

No.	Object	$z$	$f(9)$	$f(18)$	$f(90)$	$\lambda L_\lambda(9)$	$\lambda L_\lambda(18)$	$\lambda L_\lambda(90)$	IR Catalog	$f_{\text{HX}}$	$\log L_{\text{HX}}$	$N_{\text{H}}$	$f_c$	X-ray Catalog
(1)	(2)	(3)	(4)	(5)	(6)	(7)	(8)	(9)	(10)	(11)	(12)	(13)	(14)	(15)
116	Mrk 841	0.036422	0.126	0.372	...	44.11	44.27	...	(A, A, X)	5.1	44.20	0.219	...	(b)
117	Mrk 290	0.029577	0.085	0.151	...	43.65	43.70	...	(W, A, X)	3.0	43.78	0.150	...	(a)
118	Mrk 1498	0.0547	0.067	0.214	...	44.20	44.40	...	(A, A, X)	4.5	44.51	58.0	0.9905	(a)
119	2MASX J16481523–3035037	0.031	0.030	0.038	...	43.23	43.06	...	(W, W, X)	8.6	44.28	0.240	...	(a)
120	NGC 6240	0.02448	0.350	1.489	23.100	44.20	44.53	45.02	(A, A, A)	4.7	43.81	102	...	(a)
122	NGC 6300	0.003699	0.277	1.336	14.928	42.44	42.82	43.17	(A, A, A)	9.1	42.44	21.5	...	(a)
123	GRS 1734–292	0.0214	...	...	...	...	...	...	(X, X, X)	10.9	44.05	0.912	...	(a)
124	1RXS J174538.1+290823	0.111332	0.030	0.059	...	44.40	44.41	...	(W, W, X)	3.9	45.09	0.139	...	(a)
125	3C 382	0.05787	0.120	0.106	...	44.50	43.95	...	(A, I, X)	8.1	44.81	0.013	...	(b)
126**	ESO 103-035	0.013286	0.300	1.446	1.227	43.59	43.97	43.20	(A, A, A)	9.7	43.58	21.6	0.9990	(a)
127	3C 390.3	0.0561	0.090	0.242	...	44.35	44.48	...	(A, A, X)	10.1	44.88	0.120	...	(a)
128	NVSS J193013+341047	0.0629	0.130	0.254	...	44.62	44.61	...	(A, A, X)	3.3	44.50	27.6	0.9260	(a)
129	NGC 6814	0.005214	0.334	0.258	6.954	42.65	42.41	43.14	(I, A, A)	6.2	42.57	0.058	...	(b)
130	3C 403	0.059	0.093	0.215	...	44.31	44.39	...	(W, W, X)	4.1	44.53	45.0	...	(l)
131	Cyg A	0.05607	0.152	0.418	2.455	44.47	44.72	44.79	(W, A, A)	10.9	44.91	11.0	...	(a)
133	NGC 6860	0.014884	0.155	0.357	1.369	43.41	43.47	43.35	(A, A, A)	4.9	43.39	0.100	...	(m)
136	4C +74.26	0.104	0.147	0.175	...	45.13	44.90	...	(A, A, X)	5.0	45.14	0.177	...	(n)
137	Mrk 509	0.0344	0.247	0.499	...	44.35	44.35	...	(A, A, X)	9.7	44.42	0.015	...	(a)
138	IC 5063	0.011348	1.159	2.246	3.821	43.87	44.03	43.56	(I, A, A)	7.1	43.31	25.0	0.9910	(g)
139	2MASX J21140128+8204483	0.084	0.071	0.105	...	44.62	44.48	...	(A, A, X)	3.6	44.80	0.121	...	(a)
140	IGR J21247+5058	0.02	...	...	...	...	...	...	(X, X, X)	13.9	44.10	2.47	...	(a)
141	IGR J21277+5656	0.0147	0.211	0.435	...	43.53	43.55	...	(A, A, X)	2.7	43.12	1.23	...	(a)
142	RX J2135.9+4728	0.025	...	0.240	...	...	43.76	...	(X, A, X)	2.9	43.62	0.825	...	(a)
144	UGC 11871	0.026612	0.146	0.320	5.040	43.90	43.94	44.43	(A, A, A)	3.9	43.80	2.44	...	(a)
145**	NGC 7172	0.008683	0.316	0.424	8.087	43.24	43.07	43.65	(A, A, A)	12.4	43.32	8.19	0.9990	(a)
146	NGC 7213	0.005839	0.360	0.743	2.943	42.95	42.77	42.86	(A, I, A)	5.2	42.59	0.025	...	(a)
147	NGC 7314	0.00476	0.268	0.304	4.499	42.48	42.41	42.88	(I, A, A)	5.7	42.46	1.16	...	(a)
148**	NGC 7319	0.022507	0.088	0.158	0.576	43.53	43.48	43.34	(A, A, A)	4.1	43.67	86.6	0.9965	(a)
149	3C 452	0.0811	0.029	0.070	...	44.09	44.19	...	(W, W, X)	3.3	44.73	23.0	0.9360	(a)
151	MR 2251–178	0.06398	0.090	0.148	...	44.36	44.30	...	(W, W, X)	10.8	45.03	0.280	...	(a)
152	NGC 7469	0.016317	0.767	2.692	27.694	44.18	44.42	44.74	(A, A, A)	8.3	43.70	0.041	...	(b)
153	Mrk 926	0.04686	0.060	0.214	0.647	44.01	44.26	44.04	(A, A, A)	5.5	44.45	0.035	...	(a)
154	NGC 7582	0.005254	1.368	3.287	60.906	43.43	43.51	44.08	(A, A, A)	6.7	42.61	33.0	...	(o)

NOTE. — Tables 1 summarize the infrared to X-ray properties of all the 135 Swift/BAT 9 month non-blazar AGNs in Tueller et al. (2008), including 128 with MIR counterparts: (1) source No. in (Tueller et al. 2008). The sources with asterisks\*\* represent “new type” AGNs which exhibit extremely small scattered fraction ( $f_{\text{scat}} \equiv 1 - f_c \leq 0.005$ , thus  $f_c \geq 0.995$ ) suggesting the geometrically thick tori around the nuclei. (2) object name, (3) redshift, (4)–(6) infrared fluxes ( $F_\nu$ ) at 9  $\mu\text{m}$ , 18  $\mu\text{m}$ , and 90  $\mu\text{m}$  in units of Jansky (Jy), (7)–(9) infrared luminosities ( $\lambda L_\lambda$ ) at 9  $\mu\text{m}$ , 18  $\mu\text{m}$ , and 90  $\mu\text{m}$  in units of  $\text{erg s}^{-1}$ , (10) IR reference catalogs for 9  $\mu\text{m}$ , 18  $\mu\text{m}$ , and 90  $\mu\text{m}$ , (11) hard X-ray flux in the 14–195 keV band in units of  $10^{-11} \text{erg s}^{-1} \text{cm}^{-2}$ , (12) hard X-ray luminosity in the 14–195 keV band ( $\log L_{\text{HX}}$ ) in units of  $\text{erg s}^{-1}$ , (13) X-ray absorption column density ( $N_{\text{H}}$ ), (14) covering fraction in the X-ray spectrum ( $f_c$ ), and (15) the reference for the X-ray spectra (a): Winter et al. (2009a) (b): Tueller et al. (2008) (c): Noguchi et al. (2010) (d): Eguchi et al. (2011) (e): Eguchi et al. (2009) (f): Risaliti et al. (2009) (g): Turner et al. (2009) (h): Awaki et al. (2008) (i): González-Martín et al. (2011) (j): Winter et al. (2009b) (k): Itoh et al. (2008) (l): Tazaki et al. (2011) (m): Winter & Mushotzky (2010) (n): Ballantyne (2005) (o): Bianchi et al. (2009). For AGNs whose AKARI MIR fluxes are not available, we convert the infrared fluxes and luminosities with IRAS or WISE into those at 9  $\mu\text{m}$  or 18  $\mu\text{m}$  according to the formula given in Section 2.5. Columns (1), (2), (3), (11) are taken from Tueller et al. (2008) except for the redshifts of two sources, No. 13 (2MASX J02162987+5126246) and No. 53 (2MASX J06403799–4321211), which are adopted from the Swift/BAT 58 month catalog (<http://heasarc.gsfc.nasa.gov/docs/swift/results/bs58mon/>). The X-ray spectral information (columns 13–14) is basically adopted from Winter et al. (2009a), while we refer to the results obtained with *Suzaku* (Eguchi et al. 2009, 2011; Risaliti et al. 2009; Turner et al. 2009; Awaki et al. 2008; González-Martín et al. 2011; Winter et al. 2009b; Itoh et al. 2008; Tazaki et al. 2011; Winter & Mushotzky 2010; Bianchi et al. 2009) and those with *XMM-Newton* (Noguchi et al. 2010; Ballantyne 2005) whenever available. When the information is not available in Winter et al. (2009a), we refer to Tueller et al. (2008). All luminosities in this table are calculated by using the redshift given in column (3).

TABLE 2  
CORRELATION PARAMETERS BETWEEN MIR AND THE HARD X-RAY SAMPLE

Sample (1)	$N$ (2)	$\rho_L$ (3)	$\rho_f$ (4)	$P_L$ (5)	$P_f$ (6)	$a$ (7)	$b$ (8)
9 $\mu\text{m}$	126	0.82	0.60	$3.0 \times 10^{-31}$	$1.4 \times 10^{-13}$	$0.06 \pm 0.07$	$1.12 \pm 0.08$
18 $\mu\text{m}$	127	0.76	0.59	$1.7 \times 10^{-25}$	$2.4 \times 10^{-13}$	$0.02 \pm 0.07$	$1.10 \pm 0.07$
90 $\mu\text{m}$	62	0.59	0.17	$4.5 \times 10^{-7}$	$1.8 \times 10^{-1}$	$-0.21 \pm 0.10$	$1.16 \pm 0.11$

NOTE. — Correlation Properties between 14–195 keV X-ray luminosity ( $\log L_{\text{HX}}$ ) and infrared (9, 18, and 90  $\mu\text{m}$ ) luminosities ( $\log \lambda L_\lambda(9, 18, 90 \mu\text{m})$ ) to various subsample populations. (1) sample name; (2) number of sample; (3) the Spearman's Rank coefficient for luminosity correlations ( $\rho_L$ ); (4) the Spearman's Rank coefficient for flux-flux correlations ( $\rho_f$ ); (5) the standard Student  $t$ -test null significance level for luminosity correlations ( $P_L$ ); (6) the standard Student  $t$ -test null significance level for flux-flux correlations ( $P_f$ ); (7) regression intercept ( $a$ ) and its  $1\sigma$  uncertainty; (8) slope value ( $b$ ) and its  $1\sigma$  uncertainty. Equation is represented as  $Y = a + bX$ .

TABLE 3  
AVERAGE AND STANDARD DEVIATION OF  
 $\log(\lambda L_\lambda(9, 18\mu\text{m})/L_{\text{HX}})$

Sample (1)	$N$ (2)	$\bar{r}$ (3)	$\sigma$ (4)
9 $\mu\text{m}$ All	126	$-0.129 \pm 0.039$	$0.437 \pm 0.055$
Type-1	55	$-0.165 \pm 0.052$	$0.389 \pm 0.074$
Type-2(+ New Type)	71	$-0.101 \pm 0.056$	$0.470 \pm 0.079$
18 $\mu\text{m}$ All	127	$-0.080 \pm 0.042$	$0.473 \pm 0.059$
Type-1	57	$-0.141 \pm 0.060$	$0.452 \pm 0.085$
Type-2(+ New Type)	70	$-0.031 \pm 0.058$	$0.483 \pm 0.082$

NOTE. — Averages and standard deviations of  $\log(\lambda L_\lambda(9, 18 \mu\text{m})/L_{\text{HX}})$ . (1) Sample name; (2) Number of sample; (3) average of  $\log(\lambda L_\lambda(9, 18 \mu\text{m})/L_{\text{HX}})$ ; (4) standard deviation of  $\log(\lambda L_\lambda(9, 18 \mu\text{m})/L_{\text{HX}})$